On-sky results for the integrated microlens ring tip-tilt sensor

Philipp Hottinger,[1,*] Robert J. Harris,[1,2] Jonathan Crass,[3]
Philipp-Immanuel Dietrich,[4,5,6] Matthias Blaicher,[4,5] Andrew Bechter,[3] Brian Sands,[3]
Timothy Morris,[7] Alastair G. Basden,[7] Nazim Ali Bharmal,[7] Jochen Heidt,[1]
Theodoros Anagnos,[1,2] Philip L. Neureuther,[8] Martin Glück,[8] Jennifer Power,[9]
Jörg-Uwe Pott,[2] Christian Koos,[4,5,6] Oliver Sawodny,[8] and
Andreas Quirrenbach[1]

[1]*Landessternwarte, Zentrum für Astronomie der Universität Heidelberg, Königstuhl 12, 69117 Heidelberg, Germany*
[2]*Max Planck Institute for Astronomy, Königstuhl 17, 69117, Heidelberg, Germany*
[3]*Department of Physics, University of Notre Dame, 225 Nieuwland Science Hall, Notre Dame, Indiana 46556, USA*
[4]*Institute of Microstructure Technology (IMT), Karlsruhe Institute of Technology (KIT), Hermann-von-Helmholtz-Platz 1, 76344 Eggenstein-Leopoldshafen, Germany*
[5]*Institute of Photonics and Quantum Electronics (IPQ), Karlsruhe Institute of Technology (KIT), Engesserstr. 5, 76131 Karlsruhe, Germany*
[6]*Vanguard Photonics GmbH, Hermann-von-Helmholtz-Platz 1, 76344 Eggenstein-Leopoldshafen, Germany*
[7]*Department of Physics, Durham University, South Road, Durham, DH1 3LE, UK*
[8]*Institute for System Dynamics, University of Stuttgart, Waldburgstr. 19, 70563 Stuttgart, Germany*
[9]*Large Binocular Telescope Observatory, 933 N. Cherry Ave., Tucson, Arizona 85721-0009, USA*
*Corresponding author: phottinger@lsw.uni-heidelberg.de

We present the first on-sky results of the microlens ring tip-tilt sensor. This sensor uses a 3D printed microlens ring feeding six multimode fibers to sense misaligned light, allowing centroid reconstruction. A tip-tilt mirror allows the beam to be corrected, increasing the amount of light coupled into a centrally positioned single-mode (science) fiber. The sensor was tested with the iLocater acquisition camera at the Large Binocular Telescope in Tucson, Arizona, in November 2019. The limit on the maximum achieved rms reconstruction accuracy was found to be $0.19\lambda/D$ in both tip and tilt, of which approximately 50% of the power originates at frequencies below 10 Hz. We show the reconstruction accuracy is highly dependent on the estimated Strehl ratio and simulations support the assumption that residual adaptive optics aberrations are the main limit to the reconstruction accuracy. We conclude that this sensor is ideally suited to remove post-adaptive optics noncommon path tip-tilt residuals. We discuss the next steps for concept development, including optimization of the lens and the fiber, tuning of the correction algorithm, and selection of optimal science cases. © 2021 Optical Society of America

https://doi.org/10.1364/JOSAB.421459

1. INTRODUCTION

In recent decades, improvements in the performance of an increasing number of extreme adaptive optics (ExAO) systems have led to the ability to image near the diffraction limit using 8 m class telescopes [1–4]. These ExAO systems focus on achieving the best performance over a small field of view (FoV) and regularly achieve Strehl ratios (SRs) of 80% in the near-IR (NIR). One of the most prominent goals for these systems is the direct observation and characterization of exoplanets [5], for which high angular resolution and contrast are crucial. The high level of correction provided by these ExAO systems also makes it possible to efficiently couple light from the telescope directly into single-mode fibers (SMFs) [6]. SMFs have a core diameter on the order of 10 microns, which can only transport the fundamental fiber mode. As this mode is the only spatial mode transported and has a near-Gaussian intensity profile, the corresponding output beam is very stable and easy to model. SMFs also act as a spatial filter and couple very little sky background [7]. This makes them highly suitable for direct exoplanet spectroscopy [8] and interferometry [9–13]. When coupled to a high resolution spectrograph, SMFs also remove conventional modal noise, allowing an increase in the achievable radial velocity (RV) precision [14]. A number of SMF-fed spectrographs are currently under development, including iLocater at the Large Binocular Telescope (LBT) [7,15], SPHERE and CRIRES+

at the Very Large Telescope (VLT) [16], RHEA and IRD at SCExAO/Subaru [17,18], and KPIC at Keck [19].

Because the size of the fiber is on the order of the diffraction limit (λ/D, where λ is the wavelength and D is the diameter of the telescope), the alignment accuracy is highly dependent on the point-spread function (PSF) stability (see Fig. 1 for an example of relative coupling efficiency as a function of the residual tip-tilt position). Any vibrations that occur throughout the telescope system and influence the position of the PSF in the focal plane can have a large impact on performance. These variations can be caused by electrical and mechanical components such as fans and pumps, but can also be induced by wind, atmospheric distortions, and dome seeing [20]. As these variations can have both large amplitude and high frequencies, an adaptive optics (AO) system may not be able to compensate for them sufficiently and, if they can occur outside the path to the wavefront sensor (WFS), they will not be sensed. These variations can affect the performance significantly [21] and turn out to be a limiting factor when coupling into SMFs, with coupling efficiency being degraded by as much as a factor of two [22].

Besides high-order AO correction, efficient SMF-coupling therefore requires a method to accurately sense and correct induced tip-tilt variations. Traditionally, this is accomplished by detecting the PSF at the focal plane either with a fast quad-cell photodetector [23] or camera, computing the centroid position, and feeding back a corresponding error signal to a fast tip-tilt correction mirror. More advanced systems include feed-forward correction of mechanical vibration measurements with accelerometers [24] and the deployment of complex metrology systems using concurrent alignment lasers [25]. While most of these systems have been adopted at large telescopes, they all have a significant mechanical and optical footprint and throughput loss, and they tend to become complex in operation and are vulnerable to noncommon path (NCP) effects as the tip-tilt correction is performed at a different optical surface than the SMF face.

Different fiber-based photonic sensor concepts are being investigated in the community to complement conventional AO systems [26,27]. The concept presented in this work draws from Dietrich *et al.* [28], who d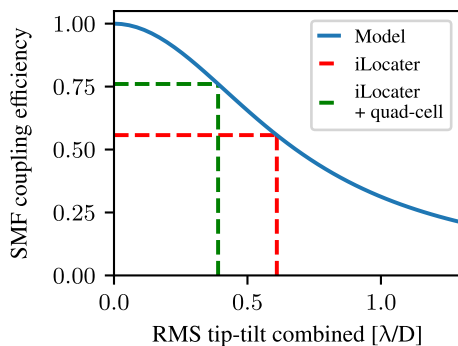eveloped a sensor with multiple single-mode (SM) cores equipped with a microlens array to refract the beam at the focal plane for both science instrument and tip-tilt sensing. Our modified concept, which is called a microlens ring tip-tilt (MLR-TT) sensor [29], features multimode fibers (MMFs) in conjunction with a microlens ring (MLR) [30] for sensing. We present the first on-sky results of this novel tip-tilt sensor with the iLocater acquisition camera at the LBT [15].

In Section 2, we describe the sensor concept and the methods used to design, manufacture, and employ it at the telescope, and also outline our simulation approach. In Section 3, we present our on-sky results and supporting simulations, and in Section 4 we discuss these results and future developments before presenting our conclusions in Section 5.

2. DESIGN AND METHODS

The MLR-TT sensor concept is depicted in Fig. 2 as both a schematic cross-section of the optics (Fig. 2, left-hand side) and as images of the manufactured components (Fig. 2, right-hand side). The details are reiterated here, with additional information, for clarity:
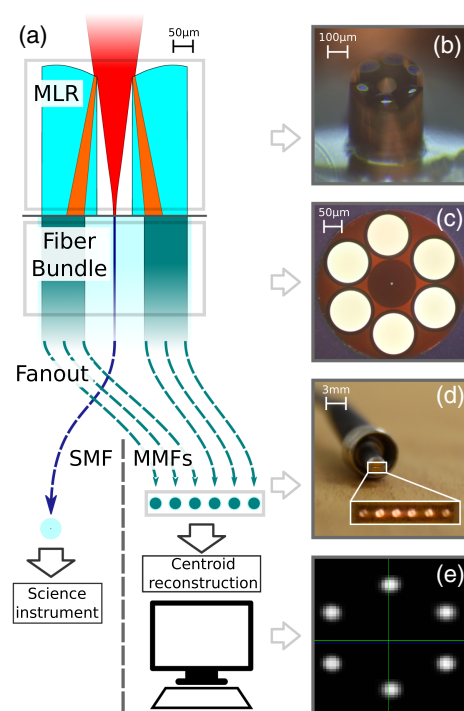
Fig. 2. Overview of the MLR-TT. (a) Schematics of the setup. The starlight (red) is coupled into the SMF (dark blue), while some light at the edges of the beam is clipped and refracted (orange beam) by the MLR (light blue) to be coupled into the sensing MMFs (dark green). The fibers are embedded in a fiber bundle that fans out into a single SMF that then feeds the starlight into a science instrument and the six MMFs that are reformatted into a linear array mounted in an SMA connector. The sensing fibers are then reimaged and the detected flux is used to reconstruct the centroid position of the telescope beam. (b) Microscope image of the MLR on the fiber bundle face. (c) Microscope image of back-illuminated fiber bundle. (d) Sensing fiber output at the fiber connector. (e) Rearranged detector signal for visual examination of the reconstruction algorithm with the green cross indicating the centroid position.

Fig. 1. Numerically calculated theoretical normalized coupling efficiency assuming an optimally coupled diffraction-limited PSF with additional residual tip-tilt variation, plotted in units of λ/D. The measured rms residuals at the iLocater focal plane are also indicated, without beam stabilization at $0.61\lambda/D$, resulting in a theoretical reduction by 44% (red line), and with additional stabilization with a quad-cell detector improving tip-tilt stability to $0.39\lambda/D$, leading to a tip-tilt induced coupling loss of 24% (green line) [15].

1. The sensor consists of a fiber bundle containing six MMFs surrounding the SMF, located at the iLocater focal plane. On the fiber face, an MLR stands 380 μm tall and 355 μm wide with a central aperture of 86 μm.
2. The central part of the beam is injected into the SMF, while the outer edge is clipped and refracted by the MLR. Depending on the alignment of the beam, the proportion of light clipped by the MLR changes, which modifies the coupling into the individual MMFs.
3. The MMFs are separated from the SMF, rearranged to form a linear array, reimaged, and read out by a detector.
4. The illumination pattern of the MMFs is processed to reconstruct the original PSF centroid position, which can be fed back to a fast steering tip-tilt mirror for correction.

A. Fiber Bundle Design

The fiber bundle was manufactured commercially (Berlin Fibre GmbH) and holds the array of seven fibers terminated into an FC/PC connector that is then connected to the iLocater fiber feed mount. The fibers are stripped of their furcation tubing and buffer and are placed in the connector with a pitch of 125 μm. After 30 cm, the SMF and the MMFs separate into two individual 5 m long fiber cables: (1) the science SMF, which is terminated to an FC/PC adapter to feed the science instrument and (2) the sensing MMFs, which are rearranged into a linear array within an SMA connector.

The SMF (Fibercore SM980) features a mode-field diameter (MFD) of 5.8 μm ($1/e^2$-intensity at 980 nm) and is taken from the same batch of the fiber that will feed the iLocater spectrograph, minimizing any fiber-to-fiber coupling losses further down the fiber link. To simplify design and production, the MMFs are off-the-shelf fibers (FG105LCA, Thorlabs Inc., Newton, NJ, USA). Their optical properties (core diameter 105 μm, NA = 0.22) were chosen to reduce the core-to-core separation between the SMF and MMFs, reducing the 3D printed lens dimensions.

B. Lens Design

The MLR design and optimization was performed using Zemax OpticStudio optical design software. To calculate the coupling efficiency into the SMF, the Physical Optics Propagation (POP) tool was employed, and for MMF coupling the Imaging tool was used. POP uses Fourier and Fresnel propagation, which is crucial when handling the near-Gaussian mode of the SMF and the complex illumination pattern on the MLR. It is computationally intensive however, so to design the shape of the lenses, the Imaging tool was used, which uses a ray-tracing algorithm to estimate the coupling efficiency into MMFs.

For our technology demonstrator, we aimed to have a strong signal for tip-tilt sensing while also enabling a high SMF coupling efficiency. This will both increase the SNR and also provide a signal in all six fibers within a reasonable dynamic range. The diameter of the central aperture was chosen to clip ∼13% of the light, reducing the maximum achievable SMF coupling efficiency with an idealized circular pupil from ∼80% [31] to ∼65%. Using this aperture, the surface shape of the

MLR was then optimized to maximize the MMF coupling efficiency, weighted to favor on-axis beams with decreasing priority for misalignment up to 100 μm (corresponding to ∼20λ/D). The surface shape of the individual lenses must provide suitable optical power to focus the incoming clipped part of the beam into the MMF. This was achieved by optimizing the spherical shape and then adding corrections with both Zernike focal sag and separate conical constants in both directions. A strong optical power was necessary to refract the beam from the inner edge of the microlens to the MMF. For this, polynomial corrections were successively applied up to fourth order in the axis parallel to the radial axis, and no additional correction was applied in the angular direction.

C. Lens Manufacturing

The MLR was manufactured using two-photon polymerization using a proprietary resin on the fiber tip [32], which allows the manufacturing of free-form lenses on a small scale. Due to the use of stages in the printing process, these structures can take arbitrary shapes, limited by the need for an appropriate support structure and macroscopic forces. The printing is aided by back-illuminating the fiber bundle and yields submicron alignment precision [28] compensating for irregularities in the bundle geometry. The process allows a precision of ∼100 nm and a rms surface roughness of ∼10 nm. The physical size was limited to the maximum build height of approximately 400 μm, due to the manufacturing stages and microscope objective numerical aperture (NA).

Once the MLR was printed on the fiber, the FC/PC connector was then placed within a bulkhead adapter (HAFC, Thorlabs, Inc., Newton, NJ, USA) for mechanical protection.

D. Laboratory Sensor Response

Because the custom lenses belonging to the iLocater acquisition camera were unavailable for laboratory experiments, the MLR-TT sensor's response was tested using commercial lenses. An SMF illuminated by a 1050 nm SLED source (S5FC1050P, Thorlabs), was apertured and a Thorlabs AC127-025-C lens was used to produce an NA of 0.14, simulating the telescope's Airy disc. The experimental system provided a lower throughput than the final on-sky experiment, due to a lower image quality. The results in Fig. 3 show the sensor's response to an gradually off-centered beam in the laboratory setup, both as modeled and as measured. The modeled SMF coupling efficiency (Fig. 3, top) includes a Fresnel reflection loss of 3.5% at both the fiber input and output face. The maximal achievable coupling efficiency within the MLR-TT sensor's SMF is measured at 59.9 ± 0.6%, which is slightly lower than the expected value of 63.2% at the given wavelength. This coupling efficiency then drops off slightly faster than expected with an off-centered beam, but features a slightly increased coupling for misalignment of up to 2.2λ/D. The causes of this behavior are still to be understood, but are likely due to fiber bundle and lens imperfections.

The response of the sensing MMFs (Fig. 3, center) follows the modeled curves well, although the six sensing MMFs are not evenly illuminated when the beam is centered. During
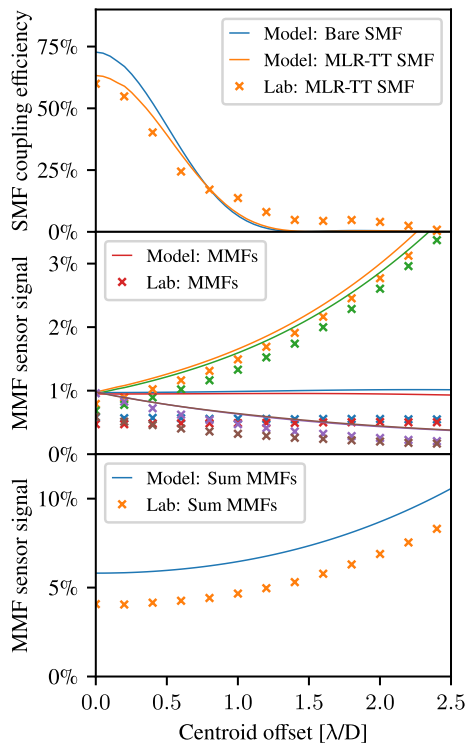
Fig. 3. Modeled (solid lines) and measured (crosses) sensor response as function of centroid offset. Top panel: the coupling efficiency of the science SMF. Middle panel: the response of the six sensing MMFs as function of beam offset. Bottom panel: MLR-TT sensor signal summed over all six MMFs.

alignment we found that the illumination pattern depends strongly on the fiber alignment angle (pitch and yaw) and could not be completely corrected. This can result from asymmetries in the beam or uneven MMF properties such as irregular spacing or different fiber losses. In practice, this is corrected by the calibration routine, as discussed in Section 2.F.

Laboratory results show the MLR couples 4.1% of the overall light into the MMFs when the beam is centered, which is 30% lower than the modeled value of 5.8% (this includes 11% reflections and losses from the fiber and 8% from the lens). Interestingly, this loss remains constant with respect to the beam
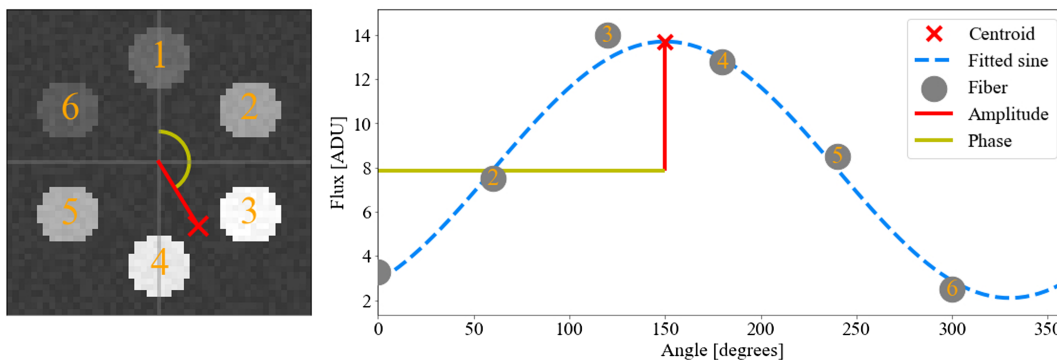
position (Fig. 3, bottom) up to a centroid offset of ∼3λ/D. We presume that the remaining mismatch is due to a nonoptimally shaped lens surface. The ray approximation as described in Section 2.B only considers a central top-hat beam but fails to accurately account for the diffractive pattern that illuminates the lenses outside the central beam.

Theoretical throughput calculations and the corresponding photon, sky background, and camera noise associated with the described system show that with this reduced sensor signal, a source with 8th magnitude in the J band can provide a SNR of 14 for each MMF output when running at 500 Hz. Simulations with the same pipeline as described in Section 2.H show that this results in an reconstruction accuracy of ∼0.1λ/D in tip and tilt combined. In this limiting case, performance is limited by read-out noise of the detector.

E. Signal Processing

The output of the sensing MMFs was reimaged with two lenses mounted within a hybrid tube and a cage mechanical system and directly attached to the lens interface of a First Light C-Red 2 InGaAs detector. This detector was chosen because it provides both a high frame rate (up to 16 kHz) and low read-out noise (34e$^-$) with a pixel size of 15 μm. Each MMF illuminates a circular region on the detector with a diameter of 100 μm. For each fiber, the 20 pixels with the highest SNR are selected and used for further processing. In laboratory tests, 20 pixels were measured to provide a steady fraction of 80% of the flux and the best overall SNR. The detector data was then processed by the Durham adaptive optics real-time controller (DARC) [33,34], running on a consumer-grade desktop computer.

F. Reconstruction and Calibration

The reconstruction algorithm shown in Fig. 4 calculates the MMF illumination and converts it to a physical centroid position. For this, the six fiber fluxes are ordered with their azimuthal coordinate and a sine function with an angular period of 2π is fitted to this signal. This routine obtains three best-fit parameters (see Fig. 4):

1. Offset, depending on both background signal and target flux;

Fig. 4. Illustration of the reconstruction routine with simulated noise. Left panel: simulated detector image showing the six MMFs (numbered 1–6 in orange) along with the reconstructed centroid of the PSF (red cross). Right panel: Graphical illustration of the reconstruction routine. Here, the six fiber fluxes (gray, numbered 1–6 in orange) are ordered by their azimuthal coordinate and a sine function with angular period of 2π is fitted, giving the angle, amplitude, and offset of the centroid.

2. Amplitude, corresponding to the radial position of the beam. Note that this is an arbitrary flux unit and the amplitude therefore does not directly yield the physical centroid position; and

3. Phase, corresponding to the azimuthal coordinate of the centroid position.

Laboratory tests showed that this approach yields the most reliable and stable output, which is less susceptible to noise than a simple center of mass (CoM) algorithm.

A calibration routine is used to correct the reconstructed centroid position for accurate loop feedback and runtime diagnostics. It accounts for irregularities in the system such as asymmetries or misalignment of the MLR, transmission variations within the fiber bundle and static aberrations in the PSF. For this, a circular motion is introduced with the tip-tilt mirror. The offset between the introduced and reconstructed azimuthal coordinate and the factor between the respective radial coordinates is approximated with individual best-fit discrete Fourier transforms (DFTs) of 5th order as a function of the azimuthal coordinate. The obtained correction function is subsequently applied to the measured centroid position. It should be noted that this calibration routine is repeated for each target to remove slowly changing quasi-static aberrations (arising from effects such as mechanical flexure) and to include asymmetries of the source itself, such as companions or background sources.

The interaction matrix is constructed by applying a linear signal in both tip and tilt with the mirror and simultaneously measuring the centroid position. The resulting 2×2 matrix is then inverted to obtain a reconstruction matrix, which can be used by the control loop to convert the measured centroid position into an feedback signal to command the tip-tilt mirror.

G. On-Sky Integration

The MLR-TT sensor was integrated into the iLocater SX acquisition camera [15] that is fed by the Large Binocular Telescope Interferometer (LBTI). The optical path is illustrated in Fig. 5. The iLocater acquisition camera receives the pupil from the telescope [Fig. 5(a)], passes the wavelengths between 920 and 950 nm [Fig. 5(c)] to its imaging channel equipped with an Andor focal plane camera (Zyla 4.2 Plus, Andor Technology Ltd., Belfast, U.K.) [Fig. 5(d)], providing a sampling of 6.1 pixels across the FWHM of the diffraction-limited PSF. This focal plane image is used as reference for the centroid position; i.e., the tip-tilt.

iLocater's native tip-tilt correction features a quad-cell photo-detector (G6849-01 InGaAs, Hamamatsu, Hamamatsu-city, Japan) [Fig. 5(g)] that is fed with light picked off by a dichroic at 1.34–1.76 μm [Fig. 5(e)], just before the final coupling optics. The quad-cell system can then feed an error signal back to a fast tip-tilt mirror (nPoint RXY3-276) [Fig. 5(b)] to correct for tip-tilt. Alternatively, the mirror can be controlled by the MLR-TT sensor to either introduce the required motions for calibration (see Section 2.F) or to correct the tip-tilt directly.

The science beam (0.97–1.31 μm) is focused by two custom triplet lenses [15] to an f/3.7 beam on the SMF to match its MFD of 5.8 μm ($1/e^2$-intensity at 970 nm). The fiber mount can be moved in five axes for alignment and to switch between three independent fibers mounted at the instrument focal plane.
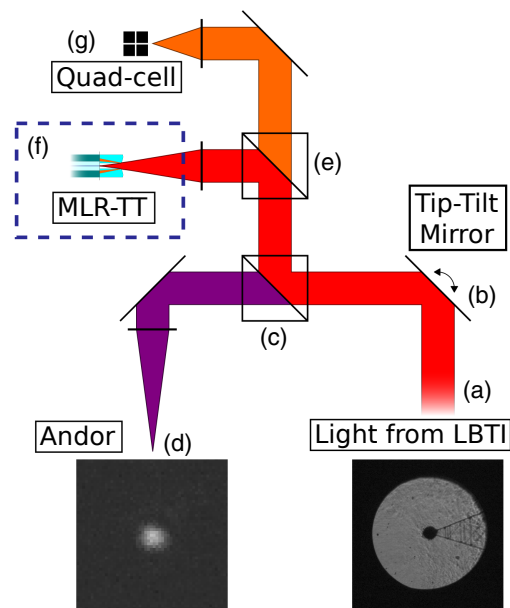

Fig. 5. Optical path of the experimental setup with the iLocater acquisition camera at LBT (sizes are not to scale). (a) Collimated AO corrected beam from LBTI is steered by (b) a fast tip-tilt mirror. (c) Short-pass dichroic transmits wavelengths between 920 and 950 nm to be imaged by (d) the Andor focal plane camera. The science light is reflected by (e) the long-pass dichroic mirror and focused into (f) the MLR-TT sensor and SMF. Light between 1.34–1.76 μm is transmitted and imaged on (g) the quad-cell that can be used in a closed loop to correct for tip-tilt vibrations.

These are: the native iLocater SMF, a bare MMF (105 μm core diameter) used for flux calibration, and the guest fiber port equipped with the MLR-TT sensor [Fig. 5(f)].

Fiber throughput is determined by measuring the output flux from each fiber with the bare MMF serving as an incident flux reference. Output flux is measured with a FemtoWatt receiver [15]. The fiber bundle holding the six sensing MMFs is routed to a separate optoelectric enclosure, housing the read-out optics and electronics.

H. Simulations of On-Sky Results

To further investigate the performance of the sensor with our recorded on-sky conditions, we simulated the sensor response for differing AO corrections. To do this, an atmospheric wavefront distortion of 1000 modes in combination with a corresponding AO system correcting 500 modes was modeled using the HCIPy high-contrast imaging simulation framework [35]. For an accurate comparison, the tip and tilt modes of the resulting wavefront are replaced by the centroid positions that were recorded during the on-sky observations.

These simulations are key because they allow us to understand our results and estimate the impact of residual AO aberrations and their dominance with respect to other noise sources.

3. RESULTS

We tested the MLR-TT on-sky in November 2019 at the LBT, using the left (SX) mirror of the telescope [15]. During the run,

the LBTI adaptive optics (LBTI-AO) system used the SOUL upgrade, which is designed to produce an SR of up to 78% in I-band [36] under optimal conditions. For all observations, the AO system was running at 1 kHz closed on 500 modes. Correction for AO noncommon path aberration (NCPA) was performed before observations, but otherwise there was no direct interaction between the MLR-TT sensor and LBTI-AO.

We present the results from three on-sky targets with a total of eight datasets. All targets were chosen to be bright (<6th magnitude), marginalizing detector noise from the MLR-TT sensor. Table 1 provides an overview of the targets, the AO loop performance, and the associated datasets.

Each dataset includes three simultaneous measurements taken using iLocater and the MLR-TT sensor:

- Andor focal plane frames (Section 2.G), taken at a frame rate of 250 Hz. A symmetric 2D Gaussian function is fitted to the data in post processing and its calculated centroid used as a reference for PSF position. The SR in Table 1 was estimated by fitting a Gaussian to the centroid-corrected PSF and taking the ratio between the normalized central intensities of this fit and the expected telescope PSF, as described in [22]. Due to the limited SNR of the individual frames, the SR calculations were smoothed by applying a moving median algorithm covering 20 frames.
- The reconstructed centroid position from the MLR-TT sensor (Section 2.F). Data were taken at a frame rate of 500 Hz. In post-processing, the frames were interpolated and cross-correlated to match the time reference of the Andor data.
- The SMF coupling efficiency was measured with the FemtoWatt receiver (Section 2.G).

A. Sensor Calibration

As described in Section 2.F, the calibration pattern was generated by introducing a circular motion on the tip-tilt mirror by issuing open loop position commands. An example of the calibration routine for target HIP7981 is shown in Fig. 6 for the Andor reference centroid position, the raw MLR-TT centroid position, and the calibrated centroid position.

During the calibration, the AO loop was closed, but no additional tip-tilt correction was applied. Due to residual vibrations at the telescope, the measured centroid positions show a broadened pattern, which is averaged. The averaged centroid positions are used to correct the reconstructed centroid for static asymmetries.
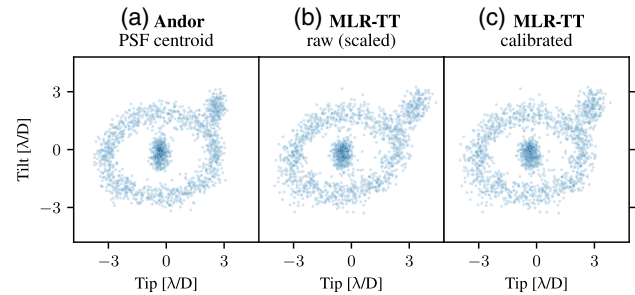

Fig. 6. Three scatter plots showing the on-sky calibration routine of target HIP7981: (a) reference centroid position measured with the Andor focal plane camera, (b) MLR-TT reconstructed raw centroid position reconstructed from the MLR-TT, and (c) calibrated MLR-TT centroid position (see Table 2). Initially the PSF is centered, then a circular motion is introduced on the fast tip-tilt mirror. This movement is not calibrated in λ/D and produces an elliptical shape in the focal plane due to the angle of the tip-tilt mirror. The introduced figure also features a central accumulation from before and after the circular motion, as well as an introduced step position seen as a separate patch to the top right of the circle.

For HIP7981, the reconstruction without calibration shows an rms error of $0.33\lambda/D$ in tip and $0.26\lambda/D$ in tilt ($0.42\lambda/D$ combined). After correction, this improves to $0.19\lambda/D$ in tip and $0.21\lambda/D$ in tilt ($0.28\lambda/D$ combined) and appears random. The impact of the calibration on the reconstruction accuracy for all targets is listed in Table 2, including the rms shift that is applied by the calibration. This shift corresponds to the correction that the calibration routine performs on the centroid position, which is seen as an improvement of the reconstructed centroid position. The correction provides a more significant improvement for the datasets with lower pre-calibration rms reconstruction errors. This arises from a more precise measurement of the calibration pattern (corresponding to a thinner ring in Fig. 6) that leads to a more accurate parametrization of the correction function.

For all other datasets listed in Table 1, the calibration was also applied but did not provide a significant improvement. These datasets all feature a smaller dynamical range and the applied shift varied between 0.06 and $0.09\lambda/D$ in tip and tilt combined. Compared to the overall noise in these datasets (see Section 2.D), the impact of the calibration is negligible.

Table 1.   Observed Targets and Datasets as Well as Observational Seeing, Estimated SR, and the Status of the Tip-Tilt Correction Loop

Target/Dataset		J-Band Mag.	Seeing (″)	Est. SR	Additional Tip-Tilt Control
HIP28634	/4	5.3	1.2 – 2.0	50 ± 6%	MLR-TT
	/5	″	″	52 ± 7%	None
HD12354	/1	5.9	1.0 – 1.4	67 ± 7%	None
	/2	″	″	67 ± 11%	MLR-TT
HIP7981	/2	3.8	1.0 – 1.4	66 ± 4%	MLR-TT
	/4	″	″	65 ± 4%	MLR-TT
	/5	″	″	65 ± 4%	MLR-TT
	/6	″	″	65 ± 4%	MLR-TT

Table 2.   Improvement Gained through the Calibration Routine[a]

Target	rms Error No Calibration [λ/D]	rms Error Calibrated [λ/D]	rms Calibration Shift [λ/D]
HIP28634/cal.	0.54	0.50	0.23
HD12354/cal.	0.42	0.31	0.27
HIP7981/cal.	0.42	0.28	0.30

[a]rms reconstruction error before and after applying the calibration is listed as well as the rms shift determined after the application of the calibration routine.

B. Closed-Loop Performance

In the datasets listed in Table 1, the acquired PSF centroid positions were used to drive the tip-tilt mirror. While the loop was operating stably, no improvement in SMF coupling was observed. The closed loop transfer function as seen by the MLR-TT sensor (Fig. 7, blue/orange) shows a significant rejection of frequencies below 15 Hz; however, this is not seen in the Andor reference camera (Fig. 7, green/red). Above 15 Hz, both the Andor and MLR-TT show the same behavior; however, the loop fails to correct for the faster disturbances. This suggests that the loop is not running at a high enough frequency for correction or the latency is too high.

C. Reconstruction Accuracy

This significant mismatch between the MLR-TT sensor and Andor reference in evaluating the loop performance must be understood. For this, we analyze the accuracy with which the sensor is able to reconstruct the centroid position. Figure 8 shows the centroid position for the Andor reference and the MLR-TT sensor for HD12354/1, as well as the corresponding reconstruction error. While the scatter of these values does not show any systematic patterns, the time series (cutout, bottom) shows that the sensor is indeed able to track the centroid position. The residual error features a mismatch, amounting to $0.19\lambda/D$ rms in both tip and tilt.
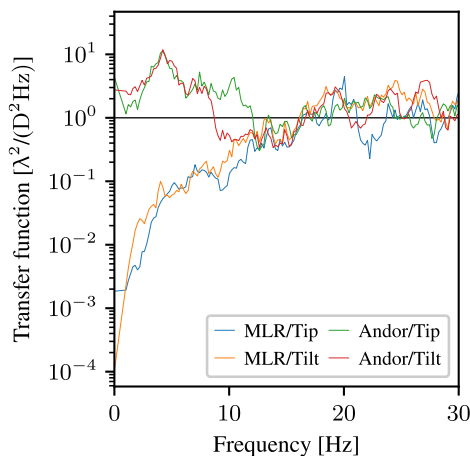

Fig. 7.   Closed loop transfer function when stabilizing the beam with the MLR-TT sensor for datasets HIP28634/4 (closed loop) and HIP28634/5. Below ~10 Hz, the MLR-TT sensor (blue, yellow) detects a different frequency rejection than the Andor reference (green, red), while above 10 Hz the transfer functions agree well.
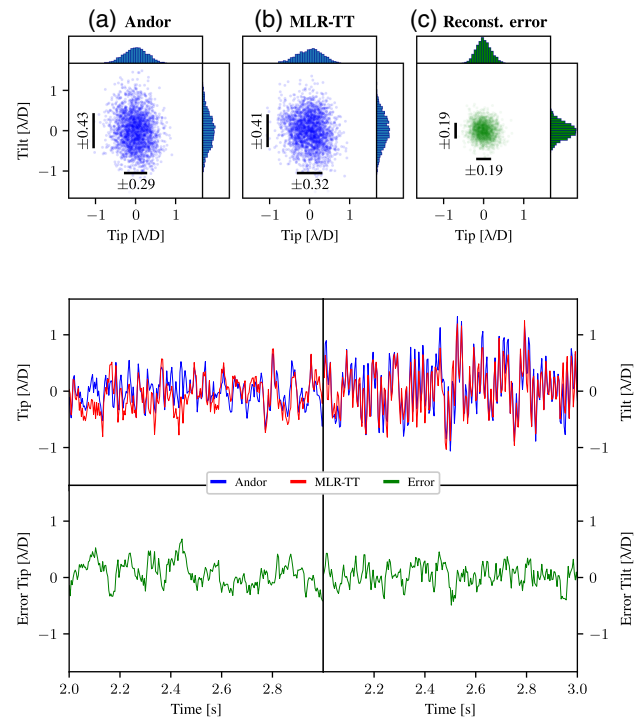

Fig. 8.   Sensor reconstruction accuracy shown graphically. Top panels: scatter plot of the recorded centroid positions; (left) measured by the Andor focal plane camera, (center) reconstructed with the MLR-TT, and (right) the error in the reconstruction by taking the difference between the former two datasets. Bottom panels: time series graphs of the same dataset for (top) comparison of the centroid x position for (tip, left) and y position (tilt, right) of Andor reference (blue) and MLR-TT (red), and (bottom) the corresponding reconstruction error (green) from their difference.

The time series of the error suggests a strong low-frequency component. The power spectral density (PSD) of the MLR-TT sensor tracks this behavior very well (see Fig. 9), with the sensor PSD tracking the features of the reference centroid very accurately above 10 Hz. Residuals below 10 Hz are calculated to account for approximately 50% of the combined tip-tilt error, while residuals between 10 and 20 Hz contribute less than 20%.

D. Impact of AO Performance

Figure 10 shows the combined tip-tilt reconstruction error for all datasets as a function of estimated SR. Note that all datasets feature similar rms centroid values (~λ/D).

The wavefront correction varies significantly between the datasets and within individual datasets, with subsets featuring SRs as low as 40% and reaching up to 80%. The reconstruction accuracy shows a strong dependency on the SR and improves significantly with increasing SR. The best reconstruction shows a combined tip-tilt rms of $0.27\lambda/D$, while the worst reconstruction reaches an rms error of $0.5\lambda/D$. A linear fit yields a slope of $-0.95 \pm 0.20\lambda/D$, an improvement in rms reconstruction accuracy of ~$0.1\lambda/D$ per 10% increase in SR.

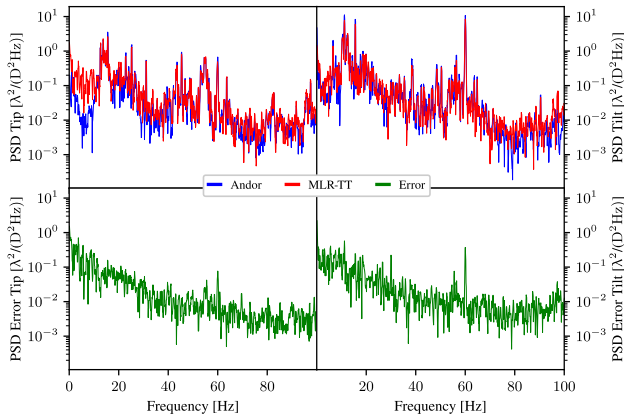**Fig. 9.** PSD for HD12354/1 of the signal shown in Fig. 8. Top: PSD of centroid x position (tip, left) and y position (tilt, right) of MLR-TT (red) compared to the Andor reference (blue). Bottom: PSD of the corresponding reconstruction error (green) for tip and tilt. Most of the vibrational power lies between 10 and 20 Hz, while most of the reconstruction error is in the low frequencies (<10 Hz).
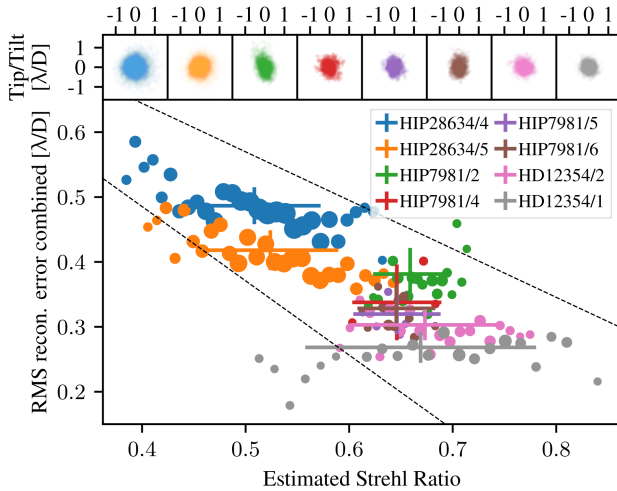

Fig. 10. On-sky sensor performance. Main panel: reconstruction accuracy as a function of estimated SR for these datasets. Cross marks in the main plot represent the mean and error for each dataset, while the circles in the subplots correspond to subsets with different estimated SRs (size of the circle represents the number of frames in each set). The dashed lines show the fitting error. Top panels: the centroid reconstruction error scatter plot for each analyzed dataset.

E. On-Sky Sensor Simulations

AO simulations as described in Section 2.H were performed to reconstruct the sensor operation. Figure 11 shows the resulting reconstruction error for tip and tilt combined as a function of the retrieved SR and is analogous to Fig. 10. For the lowest simulated SRs of ~50%, reconstruction accuracy is worse than $0.35\lambda/D$ and improves to $0.16\lambda/D$ for an SR of 80%. As with the on-sky results (cf. Fig. 10), the data are well fit by a linear trend, with a slope of $-0.72 \pm 0.05\lambda/D$. For completeness, we have also simulated the reconstruction error for a flat wavefront (Fig. 11, yellow marker) which shows a reconstruction error of less than $0.05\lambda/D$.
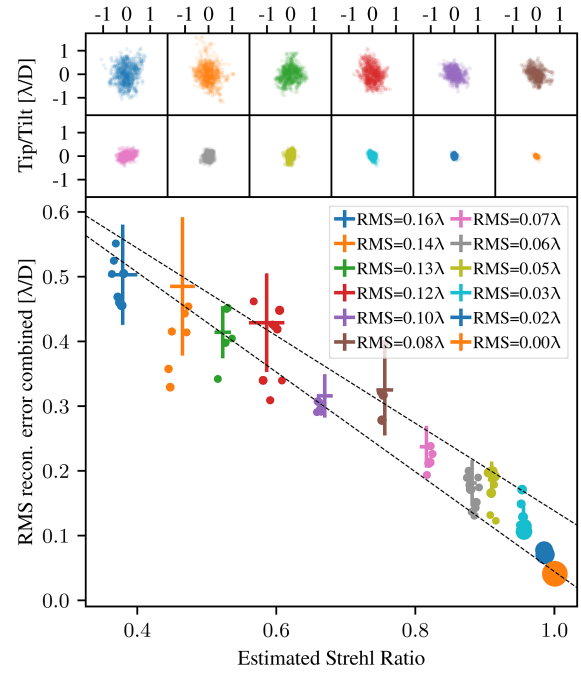

Fig. 11. Synthetic MLR-TT sensor performance derived from AO simulations, plotted to be comparable to Fig. 10. Main panel: reconstruction accuracy as a function of SR for AO simulations with varying residual aberration strength labeled with their rms wavefront error. Crosses represent overall mean and error for each data set, while the circles correspond to subsets binned by SR (size of the circle represents the number of frames in each set). The dashed lines show the fitting error. Top panels: centroid reconstruction error scatter for the individual datasets.

4. DISCUSSION

In the preceding section, we presented the on-sky performance of the MLR-TT sensor. While the sensor is able to track incident beam motions, it was unable to improve the fiber coupling performance with our current AO loop. The sensor also shows limitations in the overall performance that can be achieved due to the effects of residual aberrations. The causes and solutions are discussed in this section.

A. Sensor Reconstruction Limitations

As shown in Fig. 10, the sensor was able to reconstruct the centroid position to an accuracy of $0.27\lambda/D$ combined tip-tilt rms. The majority of this error (50%) originates in frequencies below 10 Hz and depends strongly on the estimated SR. To ascertain the cause of this error, we presented optical simulations with differing SRs in Section 3.E. The simulations show the same trend with a slightly flatter linear fit. The discrepancy can be attributed to a number of additional noise sources that occur within the measurements. These alternative sources include detector noise, reconstruction algorithm error, NCP vibrations, flux variations, and noise in the measurements of the reference centroid. While we investigated these factors during analysis, the current system is most strongly impacted by the effects of residual aberrations. For future versions of the sensor, we aim to understand the exact contributions that these noise terms have on the reconstruction accuracy.

To further investigate the impact of wavefront aberrations on the MLR-TT sensor, in future laboratory testing and on-sky experiments, we intend to acquire additional metrology data to identify other effects driving performance. This will allow us to optimize the MLR-TT reconstruction algorithm to account for the observed aberrations and possibly even reconstruct Zernike modes beyond tip and tilt.

B. Loop Performance

As illustrated in Fig. 10, under the best conditions experienced, the reconstruction accuracy of the sensor provided a combined rms error of $0.27\lambda/D$. Assuming an ideal control system, this would provide correction with an rms error 1.5 times lower than the existing quad-cell system. With our current control system, this is reduced significantly due to latency and meant the loop was only able to reject frequencies up to 15–20 Hz. The control system therefore must be optimized to allow a better correction of the tip-tilt disturbance that holds the most power in frequencies between 10 and 20 Hz (see Fig. 9).

As shown in Fig. 9, most of the noise in the reconstruction occurs below 10 Hz. The main goal will be to optimize the MLR-TT sensor software (Section 4.A) and hardware design (Section 4.C) to improve its performance in this regime. Even without additional precision, the loop can be tuned to filter this frequency range or another sensor designed to suppress vibrations in the range 1–10 Hz can be added. Alternatively, the MLR-TT sensor may be used to only detect slow beam drift below 1 Hz. Any residual aberrations will average out over long timescales (>1 s) and the sensor can be optimized to measure slow mechanical drift resulting from, e.g., gravitational flexures. This would focus the sensor on using one of its main advantages; namely, that it is virtually free from NCP effects. When running at lower frame rates, the sensor also needs less light for operation, increasing the limiting sensing magnitude and the light available for the science instrument.

C. Sensor Optimization

To control the amount of noise that is induced by residual AO aberrations, the lens design can be tuned for future devices. Because the shape of the MLR surface is set by the need to efficiently couple light into the MMFs, the height of the lens and the size of the central aperture then become the most important variables. Both parameters control the distance from the focal plane where the telescope beam is sensed and, by varying them, the impact of aberrations in the system changes.

By sampling the beam closer to the fiber focal plane, the MLR-TT sensor will use an intensity distribution more similar to the PSF for sensing, which depends mostly on the phase of the wavefront at the pupil. As the height of the MLR increases, the beam enters the Fresnel regime and the sensor is therefore also affected by variations in the pupil intensity that arise from scintillation and pupil instability. Fully analyzing this parameter space will be crucial for future sensor optimization.

The size of the lens ring aperture determines how much of the beam's central core is diverted to the sensor. Because the edges of the beam are more susceptible to higher-order modes and asymmetries, using more of the beam's core will result in

more reliable measurements. However, this will also reduce the fraction of light available for science measurements. This trade-off is the key design choice that will be determined by future use cases and implementations. In addition to the size of the central aperture, the NA can be used to slightly change the ratio between sensor signal and SMF coupling. Given the right optical system, it would be possible to perform individual adjustments of this trade-off for each observed target.

D. Future Applications

The system presented in this work was optimized to be used with the iLocater acquisition camera at the LBT; however, there are other diffraction-limited systems where the technology also can find applications. As discussed in Section 4.A, the performance is limited by residual AO aberrations, and thus the most beneficial application will be with systems that feature as little residual wavefront aberrations as possible.

In addition to current and future ExAO systems at large observatories, the MLR-TT sensor also offers an advantage for small observatories, free-space optical communications systems, and space-based applications that employ diffraction-limited telescopes. In these systems, the sensor can be integrated in a very compact fashion without the need for additional optical components in the optical train, which reduces both the complexity and mechanical footprint.

5. CONCLUSION

We presented the first on-sky results of our 3D-printed, fiber-based MLR-TT. The sensor was tested with the iLocater acquisition camera at the Large Binocular Telescope in Tucson, Arizona, in November 2019. The system consists of a 3D-printed microlens ring that uses six multimode fibers to reconstruct the centroid position, while providing an almost unobscured aperture where a science single-mode fiber is positioned. This concept features a very small optomechanical footprint and degrades the maximum single-mode fiber coupling efficiency by 15%, which is comparable to typical losses due to beam aberrations.

We showed that the fundamental principle works well and the sensor is able to reach a maximum reconstruction accuracy of $0.19\lambda/D$ in each tip and tilt; however, the system was not able to improve single-mode fiber coupling efficiency. The majority of the vibration was measured in frequencies between 10 and 20 Hz, but the majority of the reconstruction error was shown to occur in low frequencies between 1 and 10 Hz. This error in reconstructing the centroid depended strongly on the estimated SR and subsequent simulations were able to recreate this trend, suggesting that residual aberrations were the dominating noise source that limited performance.

These findings will help to tune both the optical design and reconstruction algorithm to improve centroid measurements and reduce the impact of residual aberrations. Alternatively, the respective frequency range can be filtered or corrected using another sensor to minimize its impact.

We conclude that the MLR-TT sensor is best suited for applications requiring fast correction with low higher-order wavefront distortions while benefiting from its compact

nature. This includes ExAO systems, compact systems at small diffraction-limited telescopes, and space-based applications. We also note that the MLR-TT sensor operates very close to the fiber coupling surface, it is free of noncommon path aberration and can therefore be used to track drifts and perform guiding in a closed-loop system where calibration between the wavefront sensor and fiber is difficult.

Disclosures.   The authors declare no conflicts of interest.

Data Availability.   Data underlying the results presented in this paper are not publicly available at this time but may be obtained from the authors upon reasonable request.

REFERENCES

1. J.-L. Beuzit, M. Feldt, K. Dohlen, D. Mouillet, P. Puget, F. Wildi, L. Abe, J. Antichi, A. Baruffolo, P. Baudoz, A. Boccaletti, M. Carbillet, J. Charton, R. Claudi, M. Downing, C. Fabron, P. Feautrier, E. Fedrigo, T. Fusco, J.-L. Gach, R. Gratton, T. Henning, N. Hubin, F. Joos, M. Kasper, M. Langlois, R. Lenzen, C. Moutou, A. Pavlov, C. Petit, J. Pragt, P. Rabou, F. Rigal, R. Roelfsema, G. Rousset, M. Saisse, H.-M. Schmid, E. Stadler, C. Thalmann, M. Turatto, S. Udry, F. Vakili, and R. Waters, "SPHERE: a 'Planet Finder' instrument for the VLT," Proc. SPIE **7014**, 701418 (2008).
2. S. Esposito, A. Riccardi, E. Pinna, A. Puglisi, F. Quirós-Pacheco, C. Arcidiacono, M. Xompero, R. Briguglio, G. Agapito, L. Busoni, L. Fini, J. Argomedo, A. Gherardi, G. Brusa, D. Miller, J. C. Guerra, P. Stefanini, and P. Salinari, "Large Binocular Telescope Adaptive Optics System: new achievements and perspectives in adaptive optics," Proc. SPIE **8149**, 814902 (2011).
3. B. Macintosh, J. R. Graham, P. Ingraham, Q. Konopacky, C. Marois, M. Perrin, L. Poyneer, B. Bauman, T. Barman, A. S. Burrows, A. Cardwell, J. Chilcote, R. J. De Rosa, D. Dillon, R. Doyon, J. Dunn, D. Erikson, M. P. Fitzgerald, D. Gavel, S. Goodsell, M. Hartung, P. Hibon, P. Kalas, J. Larkin, J. Maire, F. Marchis, M. S. Marley, J. McBride, M. Millar-Blanchaer, K. Morzinski, A. A. Norton, B. R. Oppenheimer, D. Palmer, J. Patience, L. Pueyo, F. Rantakyro, N. Sadakuni, L. Saddlemyer, D. Savransky, A. Serio, R. Soummer, A. Sivaramakrishnan, I. Song, S. Thomas, J. K. Wallace, S. Wiktorowicz, and S. Wolff, "First light of the Gemini Planet Imager," Proc. Natl. Acad. Sci. USA **111**, 12661–12666 (2014).
4. N. Jovanovic, F. Martinache, O. Guyon, C. Clergeon, G. Singh, T. Kudo, V. Garrel, K. Newman, D. Doughty, J. Lozi, J. Males, Y. Minowa, Y. Hayano, N. Takato, J. Morino, J. Kuhn, E. Serabyn, B. Norris, P. Tuthill, G. Schworer, P. Stewart, L. Close, E. Huby, G. Perrin, S. Lacour, L. Gauchet, S. Vievard, N. Murakami, F. Oshiyama, N. Baba, T. Matsuo, J. Nishikawa, M. Tamura, O. Lai, F. Marchis, G. Duchene, T. Kotani, and J. Woillez, "The Subaru Coronagraphic Extreme Adaptive Optics System: Enabling high-contrast imaging on solar-system scales," Publ. Astron. Soc. Pac. **127**, 890 (2015).

5. J. R. P. Angel, "Ground-based imaging of extrasolar planets using adaptive optics," Nature **368**, 203–207 (1994).
6. A. Bechter, J. Crass, R. Ketterer, J. R. Crepp, R. O. Reynolds, E. Bechter, P. Hinz, F. Pedichini, M. Foley, E. Runburg, E. E. Onuma, S. Gaudi, G. Micela, I. Pagano, and C. E. Woodward, "On-sky single-mode fiber coupling measurements at the Large Binocular Telescope," Proc. SPIE **9909**, 99092X (2016).
7. J. R. Crepp, J. Crass, D. King, A. Bechter, E. Bechter, R. Ketterer, R. Reynolds, P. Hinz, D. Kopon, D. Cavalieri, L. Fantano, C. Koca, E. Onuma, K. Stapelfeldt, J. Thomes, S. Wall, S. Macenka, J. McGuire, R. Korniski, L. Zugby, J. Eisner, B. S. Gaudi, F. Hearty, K. Kratter, M. Kuchner, G. Micela, M. Nelson, I. Pagano, A. Quirrenbach, C. Schwab, M. Skrutskie, A. Sozzetti, C. Woodward, and B. Zhao, "iLocater: a diffraction-limited Doppler spectrometer for the Large Binocular Telescope," Proc. SPIE **9908**, 990819 (2016).
8. S. Y. Haffert, R. J. Harris, A. Zanutta, F. A. Pike, A. Bianco, E. Redaelli, A. Benoît, D. G. MacLachlan, C. A. Ross, I. Gris-Sánchez, M. D. Trappen, Y. Xu, M. Blaicher, P. Maier, G. Riva, B. Sinquin, C. Kulcsár, N. A. Bharmal, E. Gendron, L. Staykov, T. J. Morris, S. Barboza, N. Muench, L. Bardou, L. Prengère, H.-F. Raynaud, P. Hottinger, T. Anagnos, J. Osborn, C. Koos, R. R. Thomson, T. A. Birks, I. A. G. Snellen, and C. U. Keller, "Diffraction-limited integral-field spectroscopy for extreme adaptive optics systems with the multicore fiber-fed integral-field unit," J. Astron. Telesc. Instrum. Syst. **6**, 045007 (2020).
9. V. Coudé du Foresto, "Integrated optics in astronomical interferometry," Symp. Int. Astron. Union **158**, 261–271 (1994).
10. J.-B. Le Bouquin, J.-P. Berger, B. Lazareff, G. Zins, P. Haguenauer, L. Jocou, P. Kern, R. Millan-Gabet, W. Traub, O. Absil, J.-C. Augereau, M. Benisty, N. Blind, X. Bonfils, P. Bourget, A. Delboulbe, P. Feautrier, M. Germain, P. Gitton, D. Gillier, M. Kiekebusch, J. Kluska, J. Knudstrup, P. Labeye, J.-L. Lizon, J.-L. Monin, Y. Magnard, F. Malbet, D. Maurel, F. Ménard, M. Micallef, L. Michaud, G. Montagnier, S. Morel, T. Moulin, K. Perraut, D. Popovic, P. Rabou, S. Rochat, C. Rojas, F. Roussel, A. Roux, E. Stadler, S. Stefl, E. Tatulli, and N. Ventura, "PIONIER: a 4-telescope visitor instrument at VLTI," Astron. Astrophys. **535**, A67 (2011).
11. S. Gillessen, F. Eisenhauer, G. Perrin, W. Brandner, C. Straubmeier, K. Perraut, A. Amorim, M. Schöller, C. Araujo-Hauck, H. Bartko, H. Baumeister, J.-P. Berger, P. Carvas, F. Cassaing, F. Chapron, E. Choquet, Y. Clenet, C. Collin, A. Eckart, P. Fedou, S. Fischer, E. Gendron, R. Genzel, P. Gitton, F. Gonte, A. Gräter, P. Haguenauer, M. Haug, X. Haubois, T. Henning, S. Hippler, R. Hofmann, L. Jocou, S. Kellner, P. Kervella, R. Klein, N. Kudryavtseva, S. Lacour, V. Lapeyrere, W. Laun, P. Lena, R. Lenzen, J. Lima, D. Moratschke, D. Moch, T. Moulin, V. Naranjo, U. Neumann, A. Nolot, T. Paumard, O. Pfuhl, S. Rabien, J. Ramos, J. M. Rees, R.-R. Rohloff, D. Rouan, G. Rousset, A. Sevin, M. Thiel, K. Wagner, M. Wiest, S. Yazici, and D. Ziegler, "GRAVITY: a four-telescope beam combiner instrument for the VLTI," Proc. SPIE **7734**, 77340Y (2010).
12. N. Cvetojevic, E. Huby, G. Martin, S. Lacour, F. Marchis, J. Lozi, N. Jovanovic, S. Vievard, O. Guyon, L. Gauchet, G. Perrin, G. Duchêne, and T. Kotani, "FIRST, the pupil-remapping fiber interferometer at Subaru telescope: towards photonic beam-combination with phase control and on-sky commissioning results (Conference Presentation)," Proc. SPIE **10701**, 107010A (2018).
13. M. A. Martinod, D. Mourard, P. Bério, K. Perraut, A. Meilland, C. Bailet, Y. Bresson, T. ten Brummelaar, J. M. Clausse, J. Dejonghe, M. Ireland, F. Millour, J. D. Monnier, J. Sturmann, L. Sturmann, and M. Tallon, "Fibered visible interferometry and adaptive optics: FRIEND at CHARA," Astron. Astrophys. **618**, A153 (2018).
14. N. Cvetojevic, N. Jovanovic, S. Gross, B. Norris, I. Spaleniak, C. Schwab, M. J. Withford, M. Ireland, P. Tuthill, O. Guyon, F. Martinache, and J. S. Lawrence, "Modal noise in an integrated photonic lantern fed diffraction-limited spectrograph," Opt. Express **25**, 25546–25565 (2017).
15. J. Crass, A. Bechter, B. Sands, D. King, R. Ketterer, M. Engstrom, R. Hamper, D. Kopon, J. Smous, J. R. Crepp, M. Montoya, O. Durney, D. Cavalieri, R. Reynolds, M. Vansickle, E. Onuma, J. Thomes, S. Mullin, C. Shelton, K. Wallace, E. Bechter, A. Vaz, J. Power, G. Rahmer, and S. Ertel, "Final design and on-sky testing of the iLocater SX acquisition camera: broadband single-mode fiber coupling," Mon. Not. R. Astron. Soc. **501**, 2250–2267 (2021).

16. A. Vigan, J.-L. Beuzit, K. Dohlen, D. Mouillet, G. Otten, E. Muslimov, M. Philipps, R. Dorn, M. Kasper, I. Baraffe, A. Reiners, and U. Seemann, "Bringing high-spectral resolution to VLT/SPHERE with a fiber coupling to VLT/CRIRES+," Proc. SPIE **10702**, 1070236 (2018).

17. T. Feger, C. Bacigalupo, T. R. Bedding, J. Bento, D. W. Coutts, M. J. Ireland, Q. A. Parker, A. Rizzuto, and I. Spaleniak, "RHEA: the ultra-compact replicable high-resolution exoplanet and Asteroseismology spectrograph," Proc. SPIE **9147**, 91477I (2014).

18. T. Kotani, M. Tamura, H. Suto, J. Nishikawa, A. Ueda, M. Kuzuhara, M. Omiya, J. Hashimoto, T. Kurokawa, T. Kokubo, T. Mori, Y. Tanaka, M. Konishi, T. Kudo, T. Hirano, B. Sato, S. Jacobson, K. Hodapp, D. Hall, M. Ishizuka, H. Kawahara, Y. Ikeda, T. Yamamuro, H. Ishikawa, K. Hosokawa, N. Kusakabe, J.-I. Morino, S. Nishiyama, N. Jovanovic, W. Aoki, T. Usuda, N. Narita, E. Kokubo, Y. Hayano, H. Izumiura, E. Kambe, M. Ikoma, Y. Hori, H. Genda, A. Fukui, Y. Fujii, H. Harakawa, M. Hayashi, M. Hidai, M. Machida, T. Matsuo, T. Nagata, M. Ogihara, H. Takami, N. Takato, H. Terada, J. Kwon, D. Oh, K. Kashiwagi, T. Nakajima, H. Baba, and G. Olivier, "The infrared Doppler (IRD) instrument for the Subaru telescope: instrument description and commissioning results," Proc. SPIE **10702**, 1070211H (2018).

19. D. Mawet, P. Wizinowich, R. Dekany, M. Chun, D. Hall, S. Cetre, O. Guyon, J. K. Wallace, B. Bowler, M. Liu, G. Ruane, E. Serabyn, R. Bartos, J. Wang, G. Vasisht, M. Fitzgerald, A. Skemer, M. Ireland, J. Fucik, J. Fortney, I. Crossfield, R. Hu, and B. Benneke, "Keck Planet Imager and Characterizer: concept and phased implementation," Proc. SPIE **9909**, 99090D (2016).

20. J. Milli, D. Mouillet, J.-L. Beuzit, J.-F. Sauvage, T. Fusco, P. Bourget, M. Kasper, K. Tristam, C. Reyes, J. H. Girard, A. Telle, C. Pannetier, F. Cantalloube, Z. Wahhaj, D. Mawet, A. Vigan, and M. N'Diaye, "Low wind effect on VLT/SPHERE: impact, mitigation strategy, and results," Proc. SPIE **10703**, 107032A (2018).

21. J. Lozi, O. Guyon, N. Jovanovic, N. Takato, G. Singh, B. Norris, H. Okita, T. Bando, and F. Martinache, "Characterizing vibrations at the Subaru Telescope for the Subaru coronagraphic extreme adaptive optics instrument," J. Astron. Telesc. Instrum. Syst. **4**, 049001 (2018).

22. A. J. Bechter, J. Crass, J. Tesch, J. R. Crepp, and E. B. Bechter, "Characterization of single-mode fiber coupling at the large binocular telescope," Publ. Astron. Soc. Pac. **132**, 015001 (2019).

23. S. Esposito, E. Marchetti, R. Ragazzoni, A. Baruffolo, J. Farinato, L. Fini, A. Ghedina, P. Ranfagni, and A. Riccardi, "Laboratory characterization of an APD-based tip-tilt corrector," Proc. SPIE **3126**, 378 (1997).

24. M. Glück, J.-U. Pott, and O. Sawodny, "Investigations of an accelerometer-based disturbance feedforward control for vibration suppression in adaptive optics of large telescopes," Publ. Astron. Soc. Pac. **129**, 065001 (2017).

25. M. Lippa, S. Gillessen, N. Blind, Y. Kok, Ş. Yazici, J. Weber, O. Pfuhl, M. Haug, S. Kellner, E. Wieprecht, F. Eisenhauer, R. Genzel, O. Hans, F. Haußmann, D. Huber, T. Kratschmann, T. Ott, M. Plattner, C. Rau, E. Sturm, I. Waisberg, E. Wiezorrek, G. Perrin, K. Perraut, W. Brandner, C. Straubmeier, and A. Amorim, "The metrology system of the VLTI instrument GRAVITY," Proc. SPIE **9907**, 990722 (2016).

26. M. Corrigan, R. J. Harris, R. R. Thomson, D. G. MacLachlan, J. Allington-Smith, R. Myers, and T. Morris, "Wavefront sensing using a photonic lantern," Proc. SPIE **9909**, 990969 (2016).

27. B. R. Norris, J. Wei, C. H. Betters, A. Wong, and S. G. Leon-Saval, "An all-photonic focal-plane wavefront sensor," Nat. Commun. **11**, 5335 (2020).

28. P.-I. Dietrich, R. J. Harris, M. Blaicher, M. K. Corrigan, T. J. Morris, W. Freude, A. Quirrenbach, and C. Koos, "Printed freeform lens arrays on multi-core fibers for highly efficient coupling in astrophotonic systems," Opt. Express **25**, 18288–18295 (2017).

29. P. Hottinger, R. J. Harris, P. I. Dietrich, M. Blaicher, A. Bechter, J. Crass, M. Glück, J. U. Pott, N. A. Bharmal, A. Basden, T. J. Morris, C. Koos, O. Sawodny, and A. Quirrenbach, "Focal plane tip-tilt sensing for improved single-mode fiber coupling using a 3D-printed microlens-ring," in *Proceedings of AO4ELT6* (2019).

30. P. Hottinger, R. J. Harris, P.-I. Dietrich, M. Blaicher, M. Glück, A. Bechter, J.-U. Pott, O. Sawodny, A. Quirrenbach, J. Crass, and C. Koos, "Micro-lens arrays as tip-tilt sensor for single mode fiber coupling," Proc. SPIE **10706**, 1070629 (2018).

31. S. Shaklan and F. Roddier, "Coupling starlight into single-mode fiber optics," Appl. Opt. **27**, 2334–2338 (1988).

32. P.-I. Dietrich, M. Blaicher, I. Reuter, M. Billah, T. Hoose, A. Hofmann, C. Caer, R. Dangel, B. Offrein, U. Troppenz, M. Moehrle, W. Freude, and C. Koos, "In situ 3D nanoprinting of free-form coupling elements for hybrid photonic integration," Nat. Photonics **12**, 241–247 (2018).

33. A. Basden, D. Geng, R. Myers, and E. Younger, "Durham adaptive optics real-time controller," Appl. Opt. **49**, 6354–6363 (2010).

34. A. G. Basden and R. M. Myers, "The Durham adaptive optics real-time controller: capability and Extremely Large Telescope suitability," Mon. Not. R. Astron. Soc. **424**, 1483–1494 (2012).

35. E. H. Por, S. Y. Haffert, V. M. Radhakrishnan, D. S. Doelman, M. Van Kooten, and S. P. Bos, "High Contrast Imaging for Python (HCIPy): an open-source adaptive optics and coronagraph simulator," Proc. SPIE **10703**, 1070342 (2018).

36. E. Pinna, S. Esposito, P. Hinz, G. Agapito, M. Bonaglia, A. Puglisi, M. Xompero, A. Riccardi, R. Briguglio, C. Arcidiacono, L. Carbonaro, L. Fini, M. Montoya, and O. Durney, "SOUL: the Single conjugated adaptive Optics Upgrade for LBT," Proc. SPIE **9909**, 99093V (2016).

37. Astropy Collaboration, T. P. Robitaille, E. J. Tollerud, P. Greenfield, M. Droettboom, E. Bray, T. Aldcroft, M. Davis, A. Ginsburg, A. M. Price-Whelan, W. E. Kerzendorf, A. Conley, N. Crighton, K. Barbary, D. Muna, H. Ferguson, F. Grollier, M. M. Parikh, P. H. Nair, H. M. Unther, C. Deil, J. Woillez, S. Conseil, R. Kramer, J. E. H. Turner, L. Singer, R. Fox, B. A. Weaver, V. Zabalza, Z. I. Edwards, K. Azalee Bostroem, D. J. Burke, A. R. Casey, S. M. Crawford, N. Dencheva, J. Ely, T. Jenness, K. Labrie, P. L. Lim, F. Pierfederici, A. Pontzen, A. Ptak, B. Refsdal, M. Servillat, and O. Streicher, "Astropy: A community Python package for astronomy," Astron. Astrophys. **558**, A33 (2013).

38. Astropy Collaboration, and A. M. Price-Whelan, B. M. Sipöcz, H. M. Günther, P. L. Lim, S. M. Crawford, S. Conseil, D. L. Shupe, M. W. Craig, N. Dencheva, A. Ginsburg, J. T. VanderPlas, L. D. Bradley, D. Pérez-Suárez, M. de Val-Borro, T. L. Aldcroft, K. L. Cruz, T. P. Robitaille, E. J. Tollerud, C. Ardelean, T. Babej, Y. P. Bach, M. Bachetti, A. V. Bakanov, S. P. Bamford, G. Barentsen, P. Barmby, A. Baumbach, K. L. Berry, F. Biscani, M. Boquien, K. A. Bostroem, L. G. Bouma, G. B. Brammer, E. M. Bray, H. Breytenbach, H. Buddelmeijer, D. J. Burke, G. Calderone, J. L. Cano Rodrguez, M. Cara, J. V. M. Cardoso, S. Cheedella, Y. Copin, L. Corrales, D. Crichton, D. D'Avella, C. Deil, É. Depagne, J. P. Dietrich, A. Donath, M. Droettboom, N. Earl, T. Erben, S. Fabbro, L. A. Ferreira, T. Finethy, R. T. Fox, L. H. Garrison, S. L. J. Gibbons, D. A. Goldstein, R. Gommers, J. P. Greco, P. Greenfield, A. M. Groener, F. Grollier, A. Hagen, P. Hirst, D. Homeier, A. J. Horton, G. Hosseinzadeh, L. Hu, J. S. Hunkeler, Ž. Ivezić, A. Jain, T. Jenness, G. Kanarek, S. Kendrew, N. S. Kern, W. E. Kerzendorf, A. Khvalko, J. King, D. Kirkby, A. M. Kulkarni, A. Kumar, A. Lee, D. Lenz, S. P. Littlefair, Z. Ma, D. M. Macleod, M. Mastropietro, C. McCully, S. Montagnac, B. M. Morris, M. Mueller, S. J. Mumford, D. Muna, N. A. Murphy, S. Nelson, G. H. Nguyen, J. Ninan, M. Nothe, S. Ogaz, S. Oh, J. Parejko, N. Parley, S. Pascual, R. Patil, A. Patil, A. Plunkett, J. Prochaska, T. Rastogi, V. R. Janga, J. Sabater, P. Sakurikar, M. Seifert, L. Sherbert, H. Sherwood-Taylor, A. Shih, J. Sick, M. Silbiger, S. Singanamalla, L. Singer, P. Sladen, K. Sooley, S. Sornarajah, O. Streicher, P. Teuben, S. Thomas, G. Tremblay, J. Turner, V. Terrón, M. V. Kerkwijk, A. D. L. Vega, L. Watkins, B. Weaver, J. Whitmore, J. Woillez, and V. Zabalza, "The Astropy Project: building an open-science project and status of the v2.0 core package," Astron. J. **156**, 18 (2018).

39. C. R. Harris, K. J. Millman, S. J. van der Walt, R. Gommers, P. Virtanen, D. Cournapeau, E. Wieser, J. Taylor, S. Berg, N. J. Smith, R. Kern, M. Picus, S. Hoyer, M. H. van Kerkwijk, M. Brett, A. Haldane, J. Fernández del Río, M. Wiebe, P. Peterson, P. Gérard-Marchant, K. Sheppard, T. Reddy, W. Weckesser, H. Abbasi, C. Gohlke, and T. E. Oliphant, "Array programming with NumPy," Nature **585**, 357–362 (2020).

40. J. D. Hunter, "Matplotlib: A 2D graphics environment," Comput. Sci. Eng. **9**, 90–95 (2007).